Chapter 3

Unravelling the obscure electronic transition and tuning of Fermi level in Cu substituted Bi_2Te_3 compound

3.1 Introduction

In the last few decades, topological insulators (TI) have gained major attention in condensed matter physics due to its unique band structure and its potential technological applications. The detailed investigation reveals, the chalcogenides and their doped compositions show non-trivial electronic bandstructure similar to the 3D TI. The physical properties of the doped compositions based on the parent chalcogenides are well investigated [40]–[65]. It has been reported that 0.3–0.5 *at.w.*% of Cu intercalation in Bi_2Se_3 shows superconductivity behaviour due to formation of Majorana Fermion[65]; 0.1–0.15 *at.w.*% of Cu substitution in Te-site of Bi_2Te_3 shows the anomalous Hall effect due to the presence of lattice defect[62] and *p*-type to *n*-type carrier transition in Cu substituted Bi_2Te_3[63] due to increase of Cu proportion. Although some of the scientific phenomena regarding the Cu-doped TI have been well addressed in recent days, few questions remain unanswered. One of such least addressed scientific phenomena in Cu-doped Bi_2Te_3 is the non-linearity

in $\rho(T)$ pattern[64]. It has been reported that low concentration Cu-doping ($\sim$ 0.1 *at.w.*% of Cu) in Bi-site of Bi_2Te_3 makes a hump-like pattern in $\rho(T)$[64]. The hump in the $\rho(T)$ constitutes, a low-T metallic-like feature to high-T semiconducting-like feature. The earlier study[64] suggests that the resistivity increases with the increase of Cu concentration of $Cu_xBi_{2-x}Te_3$ in 300–550 K range but its changing pattern with the change of Cu concentration is very complicated because of the carrier type transition. Our investigation has been started with the observation of metal-semiconductor-like transition in $\rho(T)$ of $Cu_{0.1}Bi_{1.9}Te_3$ and we try to find out the origin of such anomalous nature by exploring other experiments.

3.2 Results and discussion

3.2.1 Crystal growth and structural analysis

We have synthesized the single crystal with 5 *at.*% of Cu substitution in Bi site. Single crystalline $Bi_{1.9}Cu_{0.1}Te_3$ has been prepared by modified Bridgman method[66]. Elemental Bi(Alfa Aesar), Te(Alfa Aesar), and Cu(Alfa Aesar) with at least 99.9 % purity have been used as the starting materials. The stoichiometric amount of starting materials was take in an evacuated ($\sim 10^{-6}$ mBar) quartz ampule. The ingots were melted at 900°C in the quartz ampule and kept for 24 hr at that temperature. The liquid of the ingots was subsequently cooled to 750°C with a slow cooling rate of $2°C.hr^{-1}$ and held for three days. As the bottom edge of the quartz tube is a conical shape, the nucleation process starts from the bottom point of the quartz tube, and the crystallization process has been completed at this stage. The quartz tube is then allowed to be cooled at ambient temperature with a cooling rate of 5°C/hr. The Shiny conical shape single crystal are obtained from the quartz tube. It is very soft and easily cleavable along *ab*-plane. The small parts of the crystal have been used for further characterization.

For structural characterization using room temperature x-ray diffraction, we have used a layer of single crystal and powder of the material. We have also carried out T-dependent powder XRD in 15–300K T-range and 5–80° 2θ-range in a commercial x-ray diffrac-

tometer (model: TTRAX III, Rigaku Corp, Japan). The powders of the compound were mounted in a Cu sample holder and affirmed with the help of ultra-thin Apiezon greases. The diffractometer is attached with a Cu anode (k_α, λ = 1.5406 Å) and operated at 9kW power (V = 60 kV, I = 150 mA). The diffractograms have been taken during the heating cycle with a temperature increment rate of 5K.min^{-1}. Before obtaining any data, the sample chamber was allowed to stabilize its temperature for about 5 min. The resistivity of the synthesized compound has been measured using a physical property measurement system (model: EverCool II, Quantum Design, USA) in the T-range 5–400 K. The sample was mounted in the four-probe puck using Cu wires and silver paste. The vibrational modes of the compound have been checked using a Raman spectrometer (Model: LabRAM HR Evoloution, Horiba Ltd., Japan) attached with a CCD camera (Model: Syncerity OE) and illuminated by 633 nm laser excitation. The data obtained from Raman spectrometer in different temperatures during heating from 100–350 K in the frequency window 25–200 cm^{-1}. Laser-ARPES measurements were performed at Hiroshima Synchrotron Radiation Center (HSRC), Hiroshima, using a photon energy of 6.3 eV in ultra-high vacuum (10^{-11} torr). The fresh surfaces were prepared by cleaving the sample at 150 K and T-dependent ARPES measurement has been done at a few temperatures during heating from 150–300 K.

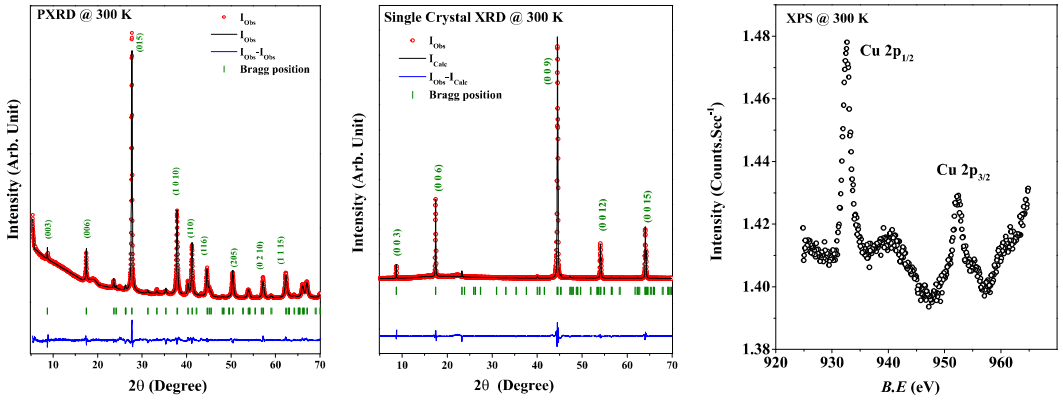

Figure 3.1: Room temperature XRD pattern of the compound $Bi_{1.9}Cu_{0.1}Te_3$; in powdered form (Left panel) and in Single crystalline form (Middle panel). Cu core level XPS spectra of Bi1.9Cu0.1Te3 (Right panel). Binding energies of Cu-$2p_{3/2}$ and Cu-$2p_{1/2}$ are similar to the pure Cu. (932.6 and 952.5 eV)

The nature of the single crystal has been confirmed from the XRD pattern (FIG. 3.1). The

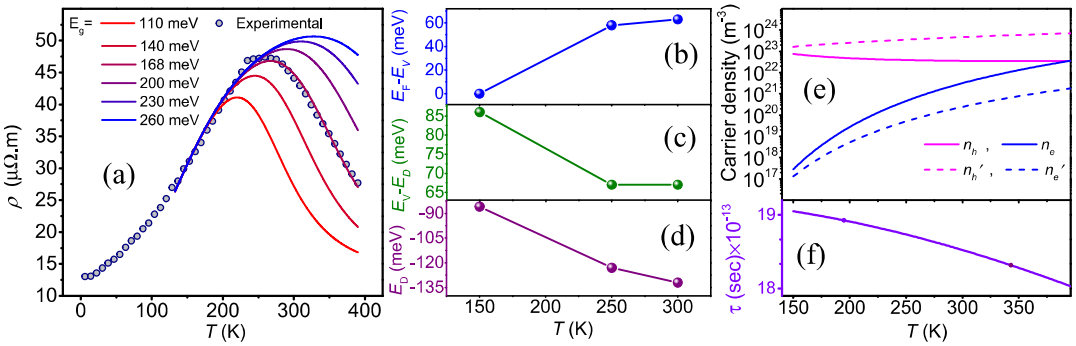

Figure 3.2: (a) Simulated $\rho(T)$ pattern with the variation of bandgap, (b) T-dependent position of the bulk valence band top, (c) T-dependent position of the bulk valence band top with respect to Dirac point energy, (d) T-dependent position of the Dirac point energy, (e) veriation of electron and hole density and (f) variation of relaxation time are shown in the figure.

occurrence of only $(00l)$ peaks in the diffractogram is well matched with the literature one[67]. The sharpness and smooth background of the data also assures the good crystalline nature of the compound. To obtain the detailed of the crystal structure, we have further performed the powder diffraction of the material (FIG. 3.1). The study suggests that the compound crystallizes in $R\bar{3}m$ crystal structure. The refinement[68], [69] of the crystal structure reveals that the lattice parameter $a = b = 4.37(2)$ Å and $c = 30.45(5)$ Å which is comparable to the lattice parameters of the pure crystal[70].

To obtain the quantitative analysis of the elements presence in the compound, we have further studied X-ray photo-emission spectroscopy (XPS)(FIG 3.1). Stoichiometric ratio calculated from the XPS analysis is very close to the experimental stoichiometric ratio.

3.2.2 Resistivity

We have synthesized the single crystal with 5 *at.*% of Cu substitution in Bi site. Single crystalline $Cu_{0.1}Bi_{1.9}Te_3$ has been prepared by modified Bridgman method[66]. The resistivity of the synthesized compound has been measured using a physical property measurement system in the T-range 5–400 K. The Laser-ARPES measurements were performed at Hiroshima Synchrotron Radiation Center (HSRC), Hiroshima, using a photon energy of 6.3 eV in ultra-high vacuum (10^{-11} torr).

$\rho(T)$ measured along the *ab* plane of the compound are shown by gray dotted line in FIG 3.2 (a). A hump in the $\rho(T)$ pattern (at 260 K), as reported earlier[64], has been observed in FIG. 3.2. We denoted 260 K, as T_P, where the peak of the resistivity is occurred. Although similar kinds of $\rho(T)$ patterns are reported[64] earlier in Cu doped Bi_2Te_3 material but the reasons yet to be clarified. It is well known that the rising of $\rho(T)$ with temperature is observed either in semiconductors at low-temperature due to impurity scattering or in the case of metals. Whereas, the decrease of $\rho(T)$ with the increase of temperature is observed in semiconductors at high-temperature due to the excitation of intrinsic carrier concentration.

Regarding the $\rho(T)$ pattern of a TI, it is observed that the surface scattering mediated by massless Dirac Fermion does not affect much in $\rho(T)$ pattern. In contrast, the bulk band (BB) has a more significant role in producing metal-semiconductor-like features in the transport phenomena. It is observed that the surface state (SS) of a TI, strongly protected by time-reversal symmetry (TRS), does not easily affected by the thermal excitation; and it remain intact beyond the room temperature[71]. In our case, too, a similar observation is performed in *T*-dependent ARPES data (discussed later). On the other hand, the BB of a TI shows a more remarkable anomaly in transport phenomena due to the unavoidable vacancies and anti-sites defects present in the crystal[72]. During its growth process, a tiny amount of defect in the pristine Bi_2Te_3 crystal can easily change its BB characteristics. In the case of Cu doped Bi_2Te_3, small variation of Cu-atom can make the material either *p*-type or *n*-type semiconductor[63]. In ARPES section, we have discussed how the BB-dependency in transport phenomena greatly contributes to our unique $\rho(T)$ pattern.

3.2.3 Temperature dependent Raman study

The layered compound Bi_2Te_3 possess $R\bar{3}m$ symmetry. The five monoatomic layers [FIG. 3.3 (a)]are covalently bond to each other. These layered are stacked in a way Te(1)-Bi-Te(2)-Bi-Te(1). The compound structure is centosymmetric with respect to Te (2) atoms, and this atom acts as an inversion center. The normal modes of vibration propagate along the trigonal *Z*-axis, and all the modes are originated from the motion of these

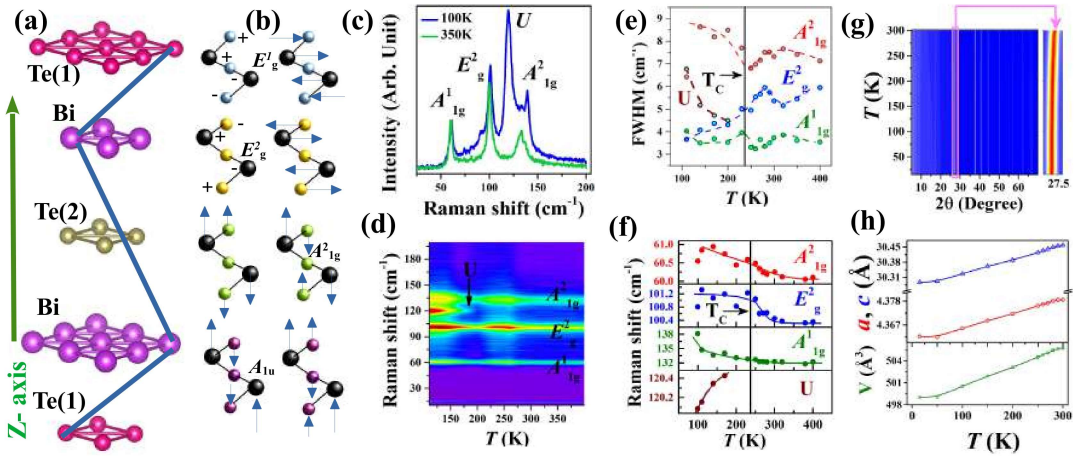

Figure 3.3: (a) Five mono atomic planes of a quintuple layer, (b) possible vibrational modes, (c) Raman spectra at 100 K and 350 K, (d)T-dependent Raman spectra as three dimensional contour plot, (e) T-dependent FWHM, (f) T-dependent mode frequency (g) The 3D contour-plot of T-dependent powder XRD pattern (enlarged view of highest-intense peak (015) are shown separately) and (h) T-dependent lattice parameters and volume are shown in the picture.

Table 3.1: Frequency of the Raman modes at 100 K and 300 K of the compound $Cu_{0.1}Bi_{1.9}Te_3$

Raman modes	Frequency (cm^{-1}) 100 K	350 K
A^1_{1g}	60.54	60.10
E^2_g	100.80	100.34
A^2_{1g}	138.11	132.20

five monoatomic layers[73]. These layers can vibrate either parallel or perpendicular to Z-axis [FIG. 3.3 (b)]. The frequency of the vibrational modes depends upon the inter-planer force for their corresponding modes. Due to inversion symmetry, all vibrational modes are exclusively either Raman active or infrared (IR) active. The $R\bar{3}m$ symmetry can produce 15 different vibrational modes, out of which 12 modes are optical, and three modes are acoustic[74]. According to the group theory classification, out of the 12 optical modes, four modes named $2A_{1g}$ and $2E_g$ are Raman active, and the rest of these are IR active. Raman active E_g modes are transverse optical mode (TO) and vibrate along the perpendicular plane of trigonal Z-axis, and A_{1g} modes are the longitudinal optical modes (LO) vibrate along the Z-axis.

From the T-dependent Raman spectroscopy we have observed A^1_{1g}, E^2_g and A^2_{1g} modes at 100 K and 350 K. The E^1_g mode is not shown because of the high background intensity. We have also observed a new Raman active mode (denoted as U) at 100 K. The Raman modes measured at 100 K, and 350 K are shown in FIG. 3.3 (c). The frequency of the modes A^1_{1g}, E^2_g and A^2_{1g} measured at 100 K and 350 K are listed in TABLE3.2.3. T-dependent Raman spectroscopy in 100–350 K is shown in three-dimensional contour plot in FIG. 3.3 (d). The T-dependent vibrational modes reveal two important facts:

First, T-dependent FWHM of the Raman modes show an anomaly at T_P. The result is remarkable regarding the metal-semiconductor phase transition. As the FWHM depends on phonon lifetime, our observation confirms that metal-semiconductor transition affects electron-phonon interaction at T_P. The change of electronic band observed in the ARPES experiment is accompanied by the vibrational change of the crystal lattice. The T-dependent FWHM is plotted in FIG. 3.3 (e). We have also figure out the T-dependent frequency of all Raman active modes [FIG. 3.3 (f)]. With the increase of T, all modes show redshift. The redshift of vibrational modes is quite natural because at high T, the interplaner spacing between the quintuple layer increases, further decreasing interplanar bonds strength. Lower bond strength lowers the vibrational frequency of phonon modes and hence the result.

Secondly, observation of a new Raman mode in the metallic phase. From FIG. 3.3 (d), it is shown that, U mode originates at 120 cm^{-1}. The frequency of U mode is very close to the frequency of the IR active A^2_u mode. It is clear from FIG. 3.3 (d), the intensity of the new mode is damped quickly as the temperature increases. At near 230 K, the intensity of the U mode almost vanishes. Such unique Raman active mode is also observed in thin film[75], [76] and electron-doped compound[77] in the same class of material, but its link with the compound's metallicity is not observed until the date. Actual reason of the U mode in the thin film is not still confirm but from the observation of the previously reported data, we can affirm that as the dimension of a particular direction is reduced it can break the lattice symmetry on that direction[75]. Another explanation of the U mode in thin film is the enhancement of the surface to volume ratio[76] which can further generate

extra charge carrier. The reduction of dimensionality is not possible in our bulk system and we can assert that the origin of the U mode in our doped TI is mainly because of the generation of extra charge carrier from *p*-type impurity band below T_P. Furthermore, we have performed T-dependent XRD [FIG. 3.3 (g)] to confirm whether the sample undergoes any structural phase transition along T_P. The result shows that there is no structural phase transition along T_P and R$\bar{3}$m space group remained maintained throughout the T-range 15–300 K. We have also plotted the T-dependent lattice parameters [FIG. 3.3 (h)] that too, does not indicate any anomaly at T_P. The whole results corroborate the fact that the metal-to-semiconductor transition rooted from electronic band structure rather than its structural phase transition.

3.2.4 Effect on magnetic field in $\rho(T)$ pattern

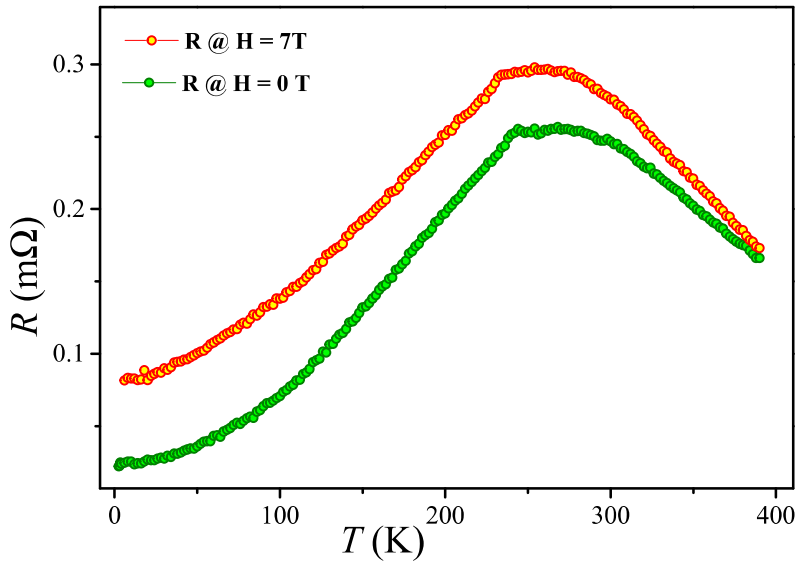

Figure 3.4: $\rho(T)$ pattern of $Cu_{0.1}Bi_{1.9}Te_3$ with (Orange) and without (Green) magnetic field

From the FIG. 3.4, it is shown that the resistivity hump shifts upward with the application of a 7 T magnetic field, but the pattern of the hump remains unaltered. It is also observed that the magnitude of the magnetoresistance is higher in low temperature which is quite natural phenomena in similar classes of the compound[78].

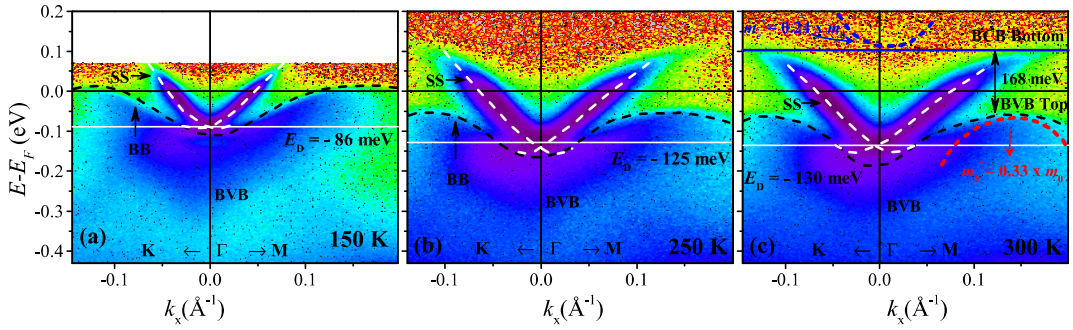

Figure 3.5: T-dependent ARPES data at (a) 150 K, (b) 250 K and (c) 300 K. The bulk valence band and the DC are shown as black and white dashed line. The solid white lines are drawn parallel to the Dirac point energy. At 300 K ARPES data, bottom edge of the bulk conduction band is shown by solid blue line to show the bulk band-gap of the compound.

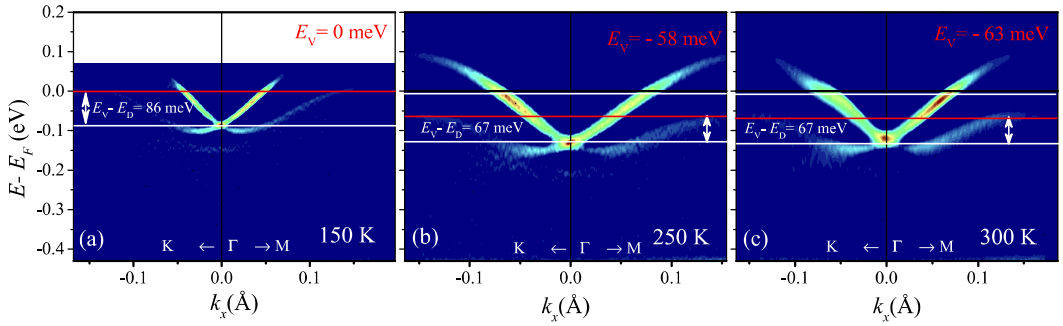

Figure 3.6: The MDC second derivative plot of the ARPES data taken at (a) 150 K; (b) 250 K, and (c) 300 K. Solid red lines are drawn parallel to the top edge of the bulk valence band. At 150 K top edge of the bulk valence band lies at Fermi level indicating the bulk metallic phase. The position of bulk valence band top with respect to Dirac point energy are indicated by white arrow.

3.2.5 ARPES study

The T-dependent angle-resolved photoelectron spectroscopy (ARPES) and its MDC (Momentum Distribution Curve) second derivative plot are shown in FIG. 3.5 and 3.6 respectively. The position of the BB and the SS in FIG. 3.5 are indicated by black and white dashed line. From 150 K ARPES data [FIG. 3.5 (a)], It is clearly visible that the Fermi level (E_F) lies at the top of the bulk valence band (BVB). It is a direct observation of the bulk metallic phase at 150 K. Above 150 K, E_F shifted toward the middle of the forbidden gap. The exact locations of the BVB top-edge (denoted as E_V) are shown by the red solid line in FIG. 3.6. It is shown that E_F-E_V (at 150 K)= 0, indicates the metallicity of the compound. In contrast, E_F-E_V at 250 K and 300 K lies at 58 and 63 meV, respectively,

translating a semiconducting phase of the compound. The result also mimics in the resistivity pattern of the compound. The T-dependency of E_F-E_V [FIG. 3.2 (b)] plays an essential role in transport phenomena, and the detailed discussions are put in the theoretical section. Such kind of BB anomaly also observed in other topological system *viz.* SnTe, where the BB observed at 22 K becomes closer to E_F at 60 K and again it shift back to higher binding energy at 120 K[79].

The position of the bulk conduction band (BCB) are marked by blue dashed line in FIG. 3.5 (c). The bottom edge of the BCB [marked by blue solid line in FIG. 3.5 (c)] is denoted as E_C. In the figure we have shown the estimated bulk bandgap (E_g) from the position of the E_V and the E_C. The red and blue dashed line in FIG. 3.5 (c) are drawn to estimate the effective mass (m^*) of the hole and the electron respectively. we have taken a double derivative (d^2E/dK^2) along the dashed lines in the ARPES data (data contains kinatic energy (E) as Y-axis and momentum (K) as X-axis) and calculated m^* by using formula $[m^*] = \frac{\hbar^2}{d^2E/dK^2}$

From T-dependent ARPES data, it is observed that the Dirac cone (DC) of the compound remains intact in the whole T-range. The presence of sharp and intense DC confirms the topological state of the TI. The fact also attests that the metal-semiconductor transition is not accompanied by the breaking of the SS. From the SS, we have evaluated the position of the Dirac point (DP). In FIG. 3.5, the position of the DP (denoted as E_D) is marked as white solid line. At 150 K, E_D = - 86 meV, and with the increase of T, E_D shifted downward. The T-dependent E_D is plotted in FIG 3.2 (d). It is shown that after 250 K, the slope of T *vs.* E_D almost flattens. The change in slope at the vicinity of T_P is the evidence of an electronic transition. The position of E_D is solely dependent on the surface-carrier density. Our result is crucial because it links how the change in BB affects the surface charge distribution. The downward shift of E_D is a result of increasing surface electron density. Although the surface carrier formation in pristine Bi_2Te_3 is reported earlier[80], its relation with the metallicity is yet to be confirmed. The charge redistribution below T_P is well verified by T-dependent Raman spectroscopy.

In FIG. 3.6, we have also figured out the position of E_V with respect to E_D (termed as E_V-E_D). The term E_V-E_D essentially tells us how the BB and the SS are interrelated to each other. The T-dependent E_V-E_D is plotted in FIG. 3.2 (c). The anomaly of slope in T *vs.* E_V-E_D again indicates an electronic transition at T_P. So far, the electronic structure is considered; it is well established that the SS and the BB are not separate from each other, and the SS originates from the BB of a TI. So, any change in the BB can effect the SS as the continuous charge transfer happens between both the states. The anomalous change of E_V-E_D at T_P results from the combined T-dependency of the SS and BB discussed earlier.

3.2.6 Drude's model and anomalous resistivity

We have already discussed the T-dependency of the bandstructure in ARPES section but, how such phenomena translates the observed $\rho(T)$ pattern is a major object of concern. In this simulation part, we have marked these issues. Our main motto of the simulation is to address all the T-dependent parameters that are evolved in the transport phenomena. Our set range of T in the simulation is 150 K to 400 K, and we want to answer how metallic bulkband at 150 K along with the T-dependent E_F can generate such unique $\rho(T)$ pattern. we also discuss quantitatively and qualitatively that how hole carrier density $n_h(T)$, electron carrier density $n_e(T)$ and the relaxation time $\tau(T)$ are changed with the change of T from 150 K to 400 K. We have started our simulation with two carrier Drude's model:

$$\rho(T) = \rho_0 + \frac{1}{\frac{n_h(T)e^2\tau(T)}{m_h^*} + \frac{n_e(T)e^2\tau(T)}{m_e^*}} \tag{3.1}$$

where,

$$\rho_0 = 13.3\ \mu\Omega m \qquad \text{(Act as a residual resistivity)} \tag{3.2}$$

$$n_h(T) = 2(\frac{2\pi m_h^* kT}{h^2})^{3/2} \times e^{-(E_F - E_V)/kT} \tag{3.3}$$

$$n_e(T) = 2(\frac{2\pi m_e^* kT}{h^2})^{3/2} \times e^{-(E_C - E_F)/kT} \tag{3.4}$$

and value of m_h^* (=0.33m_0) and m_e^* (=0.24m_0) are calculated from ARPES data. Here, $E_F - E_V$ is a function of T and increases almost linearly with T as shown in FIG3.2 (b). At 150 K, E_F lies very close to E_V; with the increase of T it is shifted towards the middle of the forbidden gap and eventually settled at 63 meV at 300 K. Similarly, the term $E_C - E_F$ (The term $E_C - E_F$ denotes the bottom position of BCB with respect to E_F) decreases with the increase of T. As the experimental E_g of our compound is 168 meV, $E_C - E_F$ changes from 168 meV at 150 K to 102 meV at 300 K. Simulated patterns of the $\rho(T)$ are shown in FIG. 3.2 (a) and it fairly matches with the experimental one from 150–400 K range. we have also predicted the $\rho(T)$-pattern with the variation of E_g from 110–230 meV. To obtain the E_g-dependent $\rho(T)$ pattern, we just vary the E_g, keeping the other parameters unchanged. The variation of n_h(T) and $n_e(T)$ are shown by solid-magenta and solid-blue line respectively in FIG. 3.2 (e)

At 150 K, n_h = 7.4×10^{22} m^{-3}, with the increase of T, n_h decreases slightly. The term n_h(T) is constituted by two T-dependent function: namely (a) $T^{3/2}$ and (b) $e^{-(E_F-E_V)/kT}$. With the increase of T, n_h tries to increase according the term (a). Now, E_F shifted upward with the increase of temperature and the term $(E_F - E_V)$ increases with the increase of T. As the term $(E_F - E_V)$ increases, n_h tries to decrease its value with the increase of T according to the the term (b). The combining effect of the both terms makes $n_h(T)$ almost flatten in the observed T-regime. If E_F remained pinned at Ev and does not move with T (unlike in our case) then $(E_F - E_V)$ = 0 for whole T-range and n_h should increase as $T^{3/2}$ (dashed-magenta line in [FIG. 3.2 (e)]). The latter example is brought to draw a relative comparison on how the shift of E_F affects the majority carrier contribution.

On the other hand, T-dependency of $n_e(T)$ is different. At 150 K, n_e = 2.8×10^{17} m^{-3}, which is much lower than the value of n_h at that T. Lower value of n_e at 150 K is accompanied by the fact that the E_C is far away from the E_F. As T increases, E_F shifted closer to the E_C which makes $e^{-(E_C-E_F)/kT}$ term growing faster. Combining the effect of $T^{3/2}$ terms, $n_e(T)$ is growing much greater than n_h in the observed T-range. Now, as the E_F is shifted towards the middle of the E_g at high T, $n_e(T)$ and $n_h(T)$ are started to contribute equally in transport phenomena. From the FIG. 3.2 (e), it is shown that the value of $n_e(T)$

becomes almost equal to value of $n_h(T)$ at 400 K. If E_F remained pinned at E_V throughout the *T*, then E_C-E_F becomes E_g (=168 meV, in our case). In such case, the rate of increase of $n_e(T)$ would lower than the previous case (Blue dotted line in FIG 3.2 (e)]).

We have also estimated the value of $\tau(T)$ from the above simulation [FIG. 3.2 (f)]. At 150 k, $\tau(T)$= 19×10^{-13} sec and it is decreasing with the increase of *T*. The falling of $\tau(T)$ with the increase of *T* is a common fact for any material. As the *T* increases, the time duration between two successive collisions decreases, and that make the downward shift of $\tau(T)$. As $\tau(T)$ is inversely proportional to the $\rho(T)$; the downfall of $\tau(T)$ is attributed to the fact of rising of the $\rho(T)$ in transport phenomena. So, the rising of $\rho(T)$ up to T_P is largely arised due to the increase of scattering incidents of the carriers. As the carrier concentration is increased exponentially with the increase of *T*, a large number of carriers start to contribute in transport phenomena. It makes the downfall of the $\rho(T)$ at high *T*-regime.

From the $\rho(T)$ simulation [FIG. 3.2 (a)], we have predicted how the variation of E_g can alter the $\rho(T)$-pattern. It is observed that, with the rise of E_g, the peak height of the $\rho(T)$ becomes higher. It is quite natural because the higher the E_g, the lesser the probability of carrier that jump from valence band to conductance band. Another interesting feature in the predicted $\rho(T)$ pattern is that, as the E_g increases, the peak position of the simulated $\rho(T)$-pattern shifted towards higher *T*. It is happening because for higher E_g it requires more thermal excitation to excite the electron from the valence band to conduction band.

3.2.7 Temperature independent scattering

The term ρ_0 does not participate in the *T*-dependent scattering phenomena. In the simulated pattern, it acts as a residual resistivity (ρ_0). We have observed that the surface transport phenomena have an enormous role in contributing ρ_0. Considering the SS of a TI, massless Dirac Fermion and its topological protection help significantly to produce such *T*-independent scattering incidents.

The thin-film study is an excellent tool to find the surface phenomena of the compound.

Table 3.2: Resistivity data for Bi_2Te_3 thin film

Thin-film growth	Resistivity ($\mu\Omega m$)	Ref:
Thermal Co-evaporation[(a)]	13.3	[81]
DC magnetron sputtering[(b)]	14.2	[82]
Nanoalloying[(c)]	9.0-33.0	[83]
Co-evaporation[(d)]	13.0	[84]

[(a)] Te/Bi ratio = 1.465 (*p*-type); measured at 363 K
[(b)] Measured along in-plane direction at 293 K
[(c)] Annealed at 523 K [(d)] Annealed at 673 K

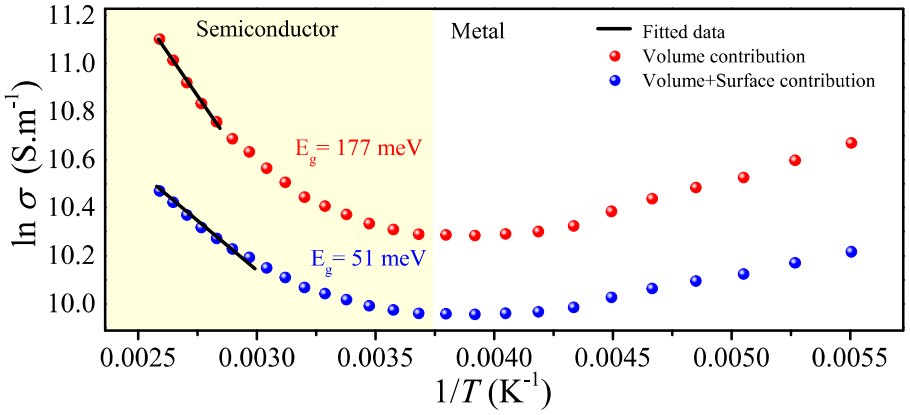

Figure 3.7: Scattering coming from the volume (red dot), volume+surface (blue dot) and corresponding fittings (black solid line) to calculate band-gap.

The resistivity study of a thin-film gives the surface-scattering information. We have confirmed the surprising fact that the theoretically predicted value of ρ_0 (13.3 $\mu\Omega$m) coming out from our best fitted parameter is very close to the surface resistivity of the pristine Bi_2Te_3 compound. The surface resistivity of pristine Bi_2Te_3 measured by thin film study is listed in a tabulated form (TABLE-3.2). Such kind of comparison strongly validates our assumption linked to the model.

We also confirm the fact that the term ρ_0 helps to estimate the actual E_g of the compound. We have plotted our data as ln σ vs. $\frac{1}{T}$ and fitted it in the semiconductor region by the equation

$$\ln\sigma = -\frac{E_g}{2k_BT} + \frac{3}{2}\ln T + \text{constant} \tag{3.5}$$

The outcome of the best-fitted parameters translates E_g = 53 meV, which is much lower

than the actual E_g of the compound. We have now, subtracted ρ_0 from our experimental resistivity data and fitted it with the above formula. The latter case translates E_g = 177 meV, which is very close to our experimental E_g (168 meV) observed in the ARPES data. Both the data along with the corresponding fitting mention above are shown in FIG. 3.7. The result corroborates that the T-dependent carrier distribution is enormously coming from the BB where ρ_0 acts as if the actual E_g becomes suppressed. The integrated results give a completeness and manifest how the combined effect of bulk and surface contribution makes a unique $\rho(T)$ pattern.

3.3 Conclusion

In conclusion we can note, the origin of the unique $\rho(T)$ pattern for the compound $Bi_{1.9}Cu_{0.1}Te_3$ has been explained using different experimental tools as well as models. Although such kind of $\rho(T)$ pattern competently recorded earlier but here some interesting facts are revealed. The evidence of electronic transition is obtained by T-dependent ARPES and Raman spectroscopy. The T dependency of E_F observed in ARPES data makes a significant contribution in observed $\rho(T)$. The simulation shows that holes mainly dominate in the metallic-like feature caused by the falling of carrier's relaxation time. With the increase of T, electron density accelerates quickly. Thermal excitation and T-dependent E_F have a significant role in enhancing the electrons' carrier density. An increase of carrier density diminishes the resistivity that further makes semiconductor-like features at a high-T regime. The simulated value of ρ_0 is very close to the surface resistivity of the pristine Bi_2Te_3. The result confirms that the T-independent scattering of the compound mainly comes from the SS of the compound and acts as a residual resistivity. The bulk bandgap can be obtained by subtracting the surface resistivity from its total contribution. The combined effect of the bulk and surface contribution make the observed $\rho(T)$ distinctive.